Composites Science and Technology **48** (1993) 237–251

ANALYSIS OF INTERFACIAL FAILURE IN A COMPOSITE MICROBUNDLE PULL-OUT EXPERIMENT

A. M. Sastry*

Sibley School of Mechanical and Aerospace Engineering, Cornell University, Ithaca, New York 14853, USA

S. L. Phoenix

Department of Theoretical and Applied Mechanics, Cornell University, Ithaca, New York 14853, USA

&

P. Schwartz

Fiber Science Program, Cornell University, Ithaca, New York 14853, USA

(Received 2 September 1992; accepted 2 November 1992)

Abstract

Modeling of the failure of polymer-matrix composites requires substantial information about the mechanisms of failure at the interface, and load redistribution around fiber breaks in the composite. Current interface experiments involving the use of 'microcomposites' of single embedded fibers in a matrix generally do not include all the key geometric features of the real composite; in particular, they do not include the effects of fiber volume fraction and the higher matrix shear resulting from closely neighboring fibers. A new experiment was recently devised to assess some of these effects: it is referred to as the single-fiber pull-out from microbundle (SFPOM) experiment. It consists of a hexagonal array of seven fibers in a matrix where the outer six fibers are restrained and the center fiber is pulled out. Recent experimental data from tests with this geometry are analyzed here using three mechanical models of the failure process, and parametric studies of the data are performed to assess the appropriateness of each model. Two of the models, based on fracture energy considerations as applied earlier to single embedded fibers in a matrix and adapted to our geometry, were found to model data from the SFPOM experiments poorly. The third model assumes the existence of three zones near a fiber break, including elastic, plastic and frictional debond zones, and was found to provide reasonable fit to the data under realistic assumptions. The reasons for persisting deviations are also discussed.

Keywords: interface, pull-out, shear lag, microcomposite

* To whom all correspondence should be addressed.

Composites Science and Technology 0266-3538/93/$06.00

NOTATION

$\mathbf{a}$	Length of a virtual mode II crack
b_{eff}	Effective fiber spacing in a hexagonal bundle
b^*_{eff}	Normalized effective fiber spacing in a hexagonal bundle
b_{min}	Nearest fiber spacing in a hexagonal bundle ($b(0)$)
b^*_{min}	Normalized nearest fiber spacing in a hexagonal bundle
$b(\theta)$	Azimuthal interfiber spacing
C	Dimensionless energy model parameter
C_{crit}	Critical energy model parameter
C_{tot}	Total energy model parameter
d	Fiber diameter
E	Fiber Young's modulus
G	Matrix shear modulus
G_c	Fracture energy per unit surface area
K	Dimensionless sample-holder geometry constant
K_1, K_2, K_3, K_4	Constants arising in three-zone shear-lag solution
l_c	Critical length of an embedded fiber
L	Embedded length
L_1	Free length above the embedded region
L_2	Free length below the embedded region

r	Fiber radius
u	Axial displacement of the center fiber
$\mathbf{U}$	Normalized axial displacement of the center fiber
U_F^t, U_F^b, U_L^m, U_L^f	Energy terms
v_f	Fiber volume fraction
w	Axial displacement of an outer fiber
$\mathbf{W}$	Normalized axial displacement of an outer fiber
z	Distance along the fiber direction
γ_D	Matrix debond shear strain
γ_Y	Matrix yield shear strain
ε_a	Applied fiber strain
ε_a^{peak}	Peak applied fiber strain
ε_{ad}	Critical fiber strain at debonding
ε_{ap}	Critical fiber strain at yielding
η	Normalized length of debond zone
θ	Normalized geometry/materials parameter
λ	Normalized embedded length
μ	Normalized length of plastic zone
ξ	Normalized axial coordinate
σ^*	Normalized stress in the fiber (to applied fiber stress)
σ_f	Normal stress in the fiber
σ_f^{ULT}	Fiber strength (assumed deterministic)
σ_{fa}	Far-field applied fiber stress
σ_{fa}^*	Normalized applied fiber stress (to fiber Young's modulus)
τ	Matrix shear stress
τ^*	Normalized matrix shear stress
τ_D	Matrix debond shear stress
τ_D^*	Normalized matrix debond shear stress
τ_Y	Matrix yeild shear stress
τ_Y^*	Normalized matrix yield shear stress
ϕ	Normalized geometry/materials parameter
Ψ	Normalized geometry/materials parameter

1 INTRODUCTION

The properties of the interface between components in a composite material have long been recognized as important factors in the determination of properties such as stiffness and strength. Characterization of these interfaces has been an area of interest to many researchers in the field in recent decades, and a wide body of literature is available on both the analytical and the experimental aspects of the problem. (See Herrera-Franco and Drzal[1] for a recent review.)

One of the earliest works on the subject was published by Cox.[2] Cox argued for the use of an elastic 'shear-lag' model, in which the full elasticity solution for a higher-modulus fiber surrounded by a lower-modulus matrix was replaced by a simplified model which regarded the surrounding matrix as a provider of only a shear stress at the interface between the fiber and matrix. Under even simpler assumptions, where the shear stress at the interface is taken as constant (as it is, for example, in a plastic matrix), Kelly and Tyson[3] used a simple force balance to determine an expression for the critical length of a strained, completely embedded fiber. At embedded lengths equal to this critical length, the fiber would fracture at its center because of the matrix shear tractions,

$$l_c = \frac{\sigma_f^{ULT} d}{2\tau_Y} \tag{1}$$

where l_c denotes the 'critical length' of fiber, σ_f^{ULT} denotes the fiber fracture stress, d denotes the fiber diameter, and τ_Y denotes the matrix yield stress. The result of this very important simplification is that the effective load transfer length of a fiber can be related in a simple way to the intrinsic properties of the components of the composite. That is, there is a particular critical length of fiber for any given fiber/matrix combination which will bear load; longer lengths will simply break at sufficiently high overall stress, as a consequence of the shear load of the matrix against the fiber at the interface.

This simple model has also been incorporated into many other models for determining interfacial behavior, in such experiments as the single-fiber composite test (SFC) in which a single fiber is encapsulated in a dogbone-shaped bar of surrounding matrix material. However, several researchers, including Netravali *et al.*,[4] have noted its limited usefulness in predicting the interfacial shear strength when mode I fracture or debonding is involved as the failure mode of the single-fiber composite specimen. Netravali *et al.*[4] found that for high-modulus epoxy composites, debonding occurred at the interface. It was also found that for the lower-modulus epoxies tested, the interface never failed; instead, failure occurred in the composite with a mode I crack in the matrix, transverse to the fiber. The observed mechanism change in the fragmentation process in SFC specimens with different constitutive behaviors for the epoxies was an important result.

Several researchers have used other types of so-called microcomposite experiments to correlate experimental parameters with interfacial failure by using criteria derived through energy analyses in a fracture mechanics setting, with simplified assumptions about the stress distribution. Specifically, Piggott,[5] Chua and Piggott[6] and Penn and Lee[7] have developed models for the prediction of the occurrence of fracture at or near the interface. These models share the same fundamental assumptions and techniques: (1) an energy balance is used to predict fracture in mode II of classic fracture mechanics, with shear-lag theory being used to calculate the stress distribution; (2) the resulting model is a function of several geometric and

material parameters, but not a function of fiber volume fraction; (3) the experiments performed to test the hypotheses involve the use of microcomposites, or specimens fabricated with only a single fiber surrounded by matrix, and where the fiber is pulled out of the matrix. Thus, the experiments in these cases were variations on the single-fiber pull-out test, in which the fiber is pulled from a thin section of epoxy with an embedded length smaller than a critical length estimated from eqn (1).

Gulino *et al.*[8] have developed a different type of interfacial model, based on experimental observations in a three-fiber graphite/glass/epoxy composite. Their model considered the effect of three possibly coexisting zones of matrix and interface along the embedded length, each with different constitutive behavior. In this model, formulation of the problem is made by using displacement and strain boundary conditions, with continuity conditions in displacement and strain applied across each constitutive zone. In the context of a classic fracture mechanics model, these zones are much larger than what is typically regarded as the 'process zone' at the crack tip, where plastic deformation is assumed to relax the stress singularity.

The choice of an appropriate interface model for use in models of macrocomposite strength is the focus of this research. Criteria in each of three models, described in the next section, are evaluated by the use of experimental results from a novel interface experiment. The models are examined for their suitability in describing the mechanics of stress transfer and debonding near broken fibers in a fiber array.

2 ANALYTICAL METHOD

The analyses described here are based on an experiment developed to give a better simulation of the *in situ* conditions of a fiber/matrix interface loaded in shear than previous methods. This test, the single-fiber pull-out from a microcomposite experiment (SFPOM experiment), developed by Qiu and Schwartz,[9] is also shown schematically in Figs 1(a) and 1(b). The nearness of the fibers to one another more closely mirrors the conditions attained in a real assembly of fibers (Fig. 1(c)). In their experiments, Qiu and Schwartz found that a debonding failure occurred in the bundle, as the Kevlar fibers used were found to have only small areas of matrix still clinging to them after being pulled out of the bundles. However, in pull-out experiments of this type with a single fiber surrounded by a large cylinder of matrix only, it was found by others that data fitted the analytic predictions derived through fracture analyses.[5–7]

Three models are examined here as possible

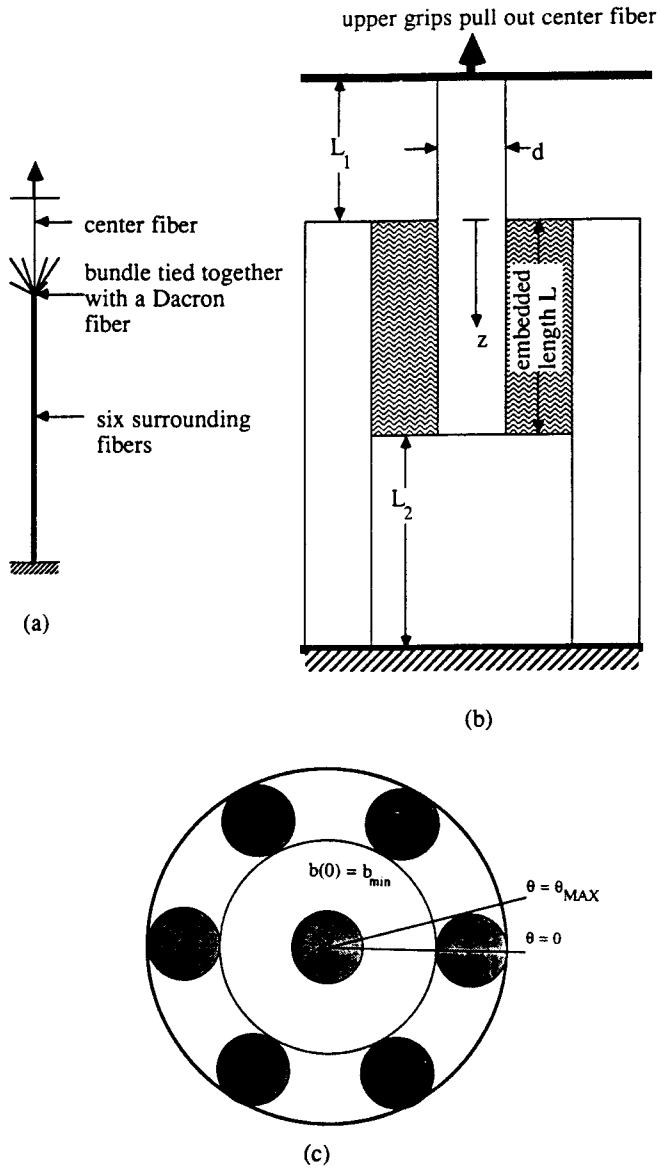

Fig. 1. SFPOM sample geometry. (a) Schematic representation of test specimen; (b) definition of geometric terms in the specimen; (c) cross-sectional schematic. (Note that in (*c*), $b(\theta)$ at $\theta > \theta_{MAX}$ is set equal to $b + 2r$.)

explanations of the behavior of the fiber pull-outs in the SFPOM experiments. Two of these are based on a fracture energy point of view, and use shear stresses in the matrix and normal stresses in the fibers derived from shear-lag considerations. Conditions for growth of mode II cracks have been derived,[5,6] and the models tested here are modifications of those models for the unique seven-fiber geometry of the SFPOM experiment.

In the first model, Piggott[5] derived the conditions for interface failure under various assumptions about the failure mechanism, including shear failure of the matrix, frictional debonding, free-length contribution of the fiber in the test grips, and mode II failure of the

interface. He assumed that all of the relevant stored elastic energy terms could be computed and then simply set equal to the total work of fracture of the interface. In the second model, Penn and Lee[7] used a Griffith-type method in which the same types of energy terms were used, but in a differential framework with respect to an assumed, initial virtual starter crack of length **a**, thus leading to a *critical* condition for crack propagation. Specifically, the sum of the derivatives with respect to **a** of each contributing energy term against the derivative of the work of fracture for the new fracture surface, and taking the limit as **a** goes to zero, gave the condition critical for crack growth. The third model, examined below, is an adaptation of the model of Gulino *et al.*[8] to the specimen geometry in the SFPOM experiment.[9] Again, shear-lag considerations were used to derive expressions for the shear stresses, but the distinguishing characteristic is the assumption that three zones of matrix and interface deformation and debonding in shear occur in succession along a fiber away from a break. In the original SFPOM experiments, insufficient data were available to directly calculate all of the model's parameters, but parametric studies based on the experimental data are performed below to assess the applicability of the model.

The analyses for the first two models proceed along similar lines and are considered first. Hereafter, Piggott's model[5] will be referred to as the 'total energy model', and the model of Penn and Lee[7] will be referred to as the 'critical energy model'. The total energy model, considered to be only an *ad hoc* curve-fitting model by Piggott,[10] is used for comparison even though the primary assumptions are called into question, as outlined in the discussion section of this paper. It yields a functional form for an interface cracking criterion that is significantly different from that of the critical energy model.

2.1 Analysis for the two fracture energy models

For the two energy models, the derivation of each of the energy terms for the SFPOM follows the method used by Piggott,[5] and is revised here for our experimental geometry. We consider the geometry shown in Fig. 1(b), with Fig. 1(c) describing a cross-section comprising both fibers and matrix. This hexagonal geometry has much in common with the geometry chosen by Greszczuk[11] and we follow his approach, although with slightly different notation.

The axial coordinate, z, is the distance along the center fiber into the composite as measured from the plane where the center fiber emerges from the matrix towards the upper grip. Following the shear-lag assumption, the center fiber stress, σ_f, satisfies the differential form

$$\frac{d\sigma_f}{dz} = \frac{2\tau_{ca}}{r} \tag{2}$$

where r is the fiber radius and τ_{ca} is the circumferential average of the shear stress at the fiber/matrix interface at fiber position z. Following Greszczuk,[11] the circumferential average is required because the shear stress on the center fiber surface will vary with azimuthal angle, θ, depending on the radial proximity to the surface of the nearest outer fiber or some characteristic distance when projecting out between fibers. On the other hand, this average shear stress, τ_{ca}, within the matrix follows the linear constitutive relationship

$$\tau_{ca} = \frac{(u-w)G}{b_{eff}} \tag{3}$$

where u is the longitudinal displacement of the center fiber, w is the longitudinal displacement of the outer fibers and G is the shear modulus of the matrix. Also following Greszczuk,[11] b_{eff} is the effective interfiber spacing radially from the surface of the center fiber to the outer fibers, as given by

$$b_{eff} = \frac{\pi}{6}\left\{\int_0^{\pi/6} \frac{d\theta}{b(\theta)}\right\}^{-1} \tag{4}$$

where $b(\theta)$ is given by

$$b(\theta) = r\left[\frac{\sin(\sin^{-1}\{(2+b_{min}/r)\sin\theta\} - \theta)}{\sin\theta} - 1\right] \tag{5}$$

for $0 < \theta < \theta_{max}$ and $b(\theta) = b_{min} + 2r$ for $\theta_{max} < \theta < \pi/6$, where

$$b_{min} = 2r\left[\left(\frac{\pi}{2(3)^{1/2}v_f}\right)^{1/2} - 1\right] \tag{6}$$

is the closest distance between fibers and v_f is fiber volume fraction. Thus $b(\theta)$ describes an outside matrix boundary as the radial distance from the surface of the center fiber to the surface of the nearest outside fiber, or to a circle circumscribing all six outside fibers when no outside fiber is in radial proximity. Figure 2 demonstrates the importance of the integration in eqn (4), particularly at high fiber volume fractions.

Normalization of the key parameters in the problem to one fiber diameter gives the following dimensionless quantities for dimensionless axial coordinate, center fiber displacement, outer fiber displacement, effective interfiber spacing and embedded length:

$$\xi \equiv \frac{z}{d} \tag{7}$$

$$\mathbf{U} \equiv \frac{u}{d} \tag{8}$$

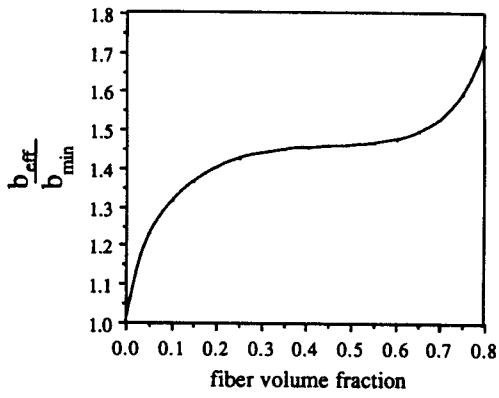

Fig. 2. Plot of (b_{eff}/b_{min}) vs. v_f.

$$\mathbf{W} \equiv \frac{w}{d} \tag{9}$$

$$b^*_{eff} = \frac{b_{eff}}{d} \tag{10}$$

$$\lambda = \frac{L}{d} \tag{11}$$

Coupled differential equations of motion for the center fiber and the outer fibers can then be written in terms of normalized fiber displacements in the wholly elastic situations of the fracture energy methods. Eliminating τ_{ca} by combining eqns (2) and (3), normalizing variables as in eqns (7)–(11), and taking a derivative with respect to ξ while eliminating $\mathbf{U}$ through substitution of the fiber constitutive equation (where σ_f denotes the center fiber stress)

$$\sigma_f = E\frac{du}{dz} = E\frac{d\mathbf{U}}{d\xi} \tag{12}$$

leads to the equations

$$\mathbf{U}'' + 2\phi(\mathbf{W} - \mathbf{U}) = 0 \tag{13}$$

$$\mathbf{W}'' + 2\theta(\mathbf{U} - \mathbf{W}) = 0 \tag{14}$$

where the double prime denotes the second derivative with respect to the normalized axial coordinate ξ, and ϕ and θ are defined below.

Because of the presence of the free lengths in the specimen, the real geometry approximates that shown in Fig. 3. For purposes of solving the strain and displacement boundary value problem, the scheme of Fig. 4 was used, as it yields stresses as in Fig. 3.

Application of the four boundary conditions

$$\xi = 0: \quad \mathbf{U}' = \varepsilon_a \tag{15a}$$

$$\mathbf{W}' = 0 \tag{15b}$$

$$\xi = \lambda: \quad \mathbf{U}' = 0 \tag{15c}$$

$$\mathbf{W} = 0 \tag{15d}$$

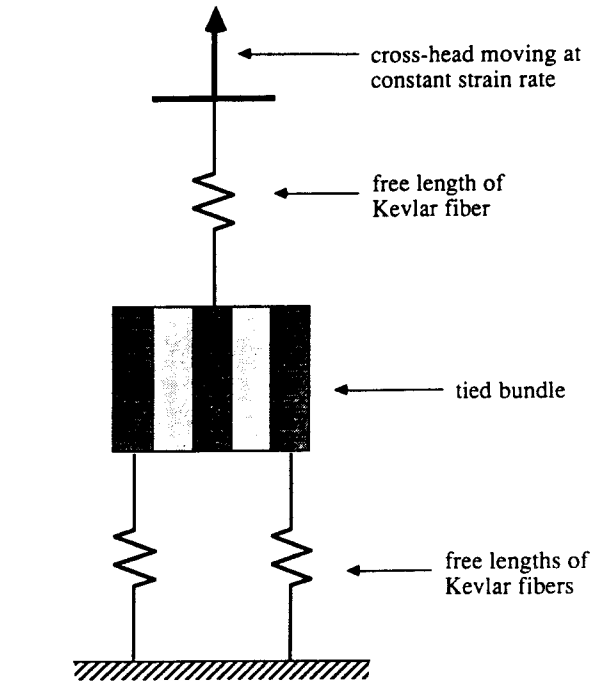

Fig. 3. Schematic of the three-zone model: schematic of actual situation in the presence of free lengths in the specimen.

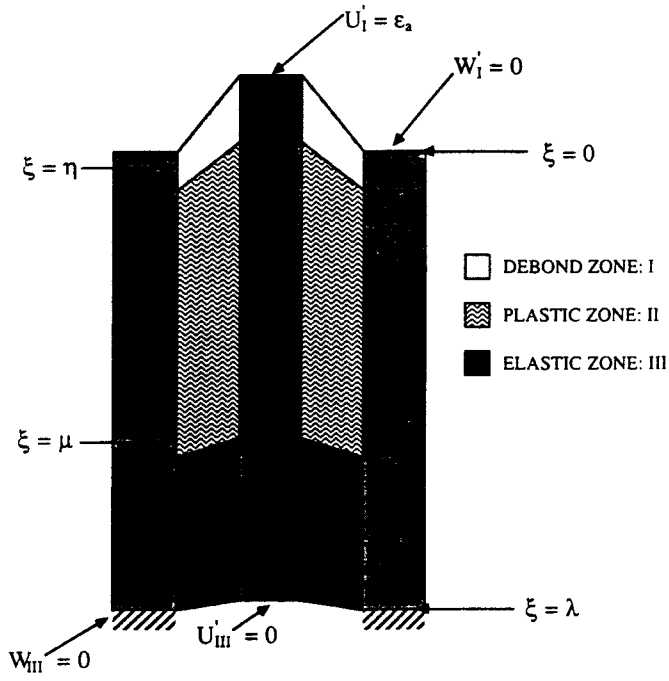

Fig. 4. Normalized coordinate system for the wholly elastic case with the boundary conditions of eqns (15).

leads to the following solution for σ^* (normalized fiber stress):

$$\sigma^* = \frac{\sigma_f}{E\varepsilon_a} = \frac{1}{\varepsilon_a}\frac{dU}{d\xi} = \frac{\frac{-\theta}{\phi}\sinh(\Psi\xi) - \sinh[\Psi(\xi-\lambda)] + \frac{\theta}{\phi}\sinh(\Psi\lambda)}{\left[1+\frac{\theta}{\phi}\right]\sinh(\Psi\lambda)} \quad (16)$$

Materials and geometry constants ϕ and θ follow, in the special geometry where the six surrounding fibers each have shear tractions applied through the matrix to only 60° of their circumferences and the center fiber has shear tractions, applied over its entire circumference (that is, the shear force on each outer fiber is one-sixth of that on the inner fiber)

$$\phi = \frac{2G}{Eb^*_{eff}} \quad (17)$$

$$\theta = \frac{G}{3Eb^*_{eff}} \quad (18)$$

$$\Psi \equiv [2(\theta+\phi)]^{1/2} \quad (19)$$

We also define the following normalized applied peak strain arising in the fracture energy solutions:

$$\varepsilon^*_a \equiv \varepsilon_a\left(\frac{Ed}{G_c}\right)^{1/2} \quad (20)$$

where G_c is the usual work of fracture per unit area of the crack in mode II.

From eqns (2) and (16), the resulting expression for the shear stress along the center fiber is obtained:

$$\tau^* = \frac{\tau_{ca}}{E\varepsilon_a} = \frac{1}{4\varepsilon_a}\frac{d^2U}{d\xi^2} = \frac{\frac{-\theta\Psi}{\phi}\cosh(\Psi\xi) - \Psi\cosh[\Psi(\xi-\lambda)]}{4\left[1+\frac{\theta}{\phi}\right]\sinh(\Psi\lambda)} \quad (21)$$

This is a normalized shear stress based on a circumferential average around the center fiber. Again following Greszczuk,[11] the peak shear stress on the center fiber occurs at the six equi-spaced circumferential positions where the radial distance to an outer fiber is the smallest value b_{min}, as indicated in Fig. 1(c). This shear stress is easily obtained from a modification of eqn (3) to be

$$\tau_{max} = \frac{(u-w)G}{b_{min}} \quad (22)$$

which, from eqns (3) and (22), is

$$\tau_{max} = \tau_{ca}\frac{b_{eff}}{b_{min}} \quad (23)$$

where σ_{fa} is the stress applied to the center fiber at the clamp.

The stress profile in the outer fibers, σ_{fo}, is given simply by

$$\sigma_{fo} = (\sigma_{fa} - \sigma_f)/6 \quad (24)$$

where σ_f is given by eqn (15), and of course $\sigma_{fo} = \sigma_{fa}/6$ in the bottom free lengths.

From these expressions, the various elastic energy terms can be evaluated. Overall, the energies of interest are the stored elastic energies in the embedded length, U_L, and in the free lengths, U_F. There is, in this case, a free fiber contribution from both the top and the bottom of the embedded length, as shown in Fig. 1(b). Each of these terms in turn is composed of several terms. For the stored extensional energy in the embedded length, U_L, we have

$$U_L = U_L^{f,center} + U_L^{f,outer} + U_L^m \quad (25)$$

where the superscripts refer in succession to the center fiber, the outer fibers and the matrix. For the energy stored in the free lengths, U_F, we have

$$U_F = U_F^{t,center} + U_F^{b,outer} \quad (26)$$

where the superscripts refer in succession to the center fiber (going to the top clamp), and the outer fibers (going to the bottom clamp).

In terms of the fiber and matrix stresses given by eqns (3), (16), (21) and (24), we calculate the various terms as follows:

$$U_L^{f,center} = \frac{\pi r^2}{2E}\int_0^L \sigma_f^2\,dz = \frac{\pi d^3 E\varepsilon_a^2}{8}\int_0^\lambda \sigma^{*2}\,d\xi \quad (27)$$

$$U_L^{f,outer} = U_L^{f,center}/6 \quad (28)$$

$$U_L^m = \pi r\int_0^L \tau_{ca}(u-w)\,dz = \frac{\pi d^2E^2\varepsilon_a^2 b^*_{eff}}{2G}\int_0^\lambda \tau^{*2}\,d\xi \quad (29)$$

$$U_F^{t,center} = \frac{\varepsilon_a^2\pi d^2 EL_1}{8} \quad (30)$$

$$U_F^{b,outer} = \frac{\varepsilon_a^2\pi d^2 EL_2}{48} \quad (31)$$

For the *total energy model*, the various terms are summed and set equal to the total work of fracture of the interface, which is $2\pi rLG_c$.

$$G_c(2\pi rL) = U_L + U_F \quad (32)$$

which results in the normalized center fiber peak strain

$$\varepsilon^*_a = (8)^{1/2}\left\{\left[\frac{7}{6\lambda}\right]\left[\frac{1}{\left(1+\frac{\phi}{\theta}\right)^2\sinh^2(\Psi\lambda)}\right]\right.$$

$$\left.\times\left[\frac{-\lambda}{2}\left(1+\left(\frac{\phi}{\theta}\right)^2\right) - \lambda\left(\frac{\phi}{\theta}\right)\cosh(\Psi\lambda) + \frac{1}{\Psi}\left(2-\frac{\phi}{\theta}\right)\right.\right.$$

$$\times \sinh(\Psi\lambda) + \lambda \sinh^2(\Psi\lambda) + \frac{1}{2\Psi}$$
$$\times \left(-3 + 4\left(\frac{\phi}{\theta}\right) + \left(\frac{\phi}{\theta}\right)^2\right) \sinh(\Psi\lambda)\cosh(\Psi\lambda)\Big]$$
$$\times \left[\frac{1}{\lambda}\right]\left[\frac{1}{\left(1+\frac{\phi}{\theta}\right)\sinh^2(\Psi\lambda)}\right]$$
$$\times \left[\left(1+\left(\frac{\phi}{\theta}\right)^2\right)\left(\frac{\lambda}{2}+\frac{1}{\Psi}\sinh(\Psi\lambda)\cosh(\Psi\lambda)\right)\right]$$
$$+\frac{\phi}{\theta}\left[\lambda\cosh(\Psi\lambda)+\frac{1}{2\Psi}\sinh(\Psi\lambda)\right]+K\Bigg\}^{-1/2} \quad (33)$$

The constant K is essentially a sample holder-geometry constant, and is given by

$$K \equiv \frac{L_1 + L_2/6}{L} \quad (34)$$

The resulting expression for the fracture of a composite microbundle with the geometry of the SFPOM experiment differs from Piggott's original expression[5] in that we include extra terms for the energy stored in the free lengths of the fibers, which leads to the constant K. In the geometry of the SFPOM samples, the value of the constant K overwhelmed the other terms in magnitude in the expression for ε_a^*. In analysis of the data we arbitrarily took $K = 0$, so that the data could be reasonably fitted. Inclusion of the term K would have resulted in virtually a constant for the right-hand side of eqn (33), regardless of changing the geometry in the SFPOM samples. It should be noted further that the constant G_c is by necessity a fitted parameter for a given matrix/fiber combination, but can be studied by matching different parameters among experiments to the governing equation, and back-calculating its value.

For the *critical energy model* of Penn and Lee[7] applied to this geometry, we replace L by the quantity $(L - \mathbf{a})$ in the energy terms given by eqns (26)–(28) and replace L_1 by $L_1 + \mathbf{a}$ in eqn (30), as the initiating crack of length $\mathbf{a}$ exists between $z = 0$ and $z = \mathbf{a}$. Next, we sum these modified terms to obtain the total elastic energy, $U_L + U_F$, for given $\mathbf{a}$. We then take a derivative with respect to $\mathbf{a}$ and set this equal to the work of fracture per unit change in length $\mathbf{a}$, which is $2\pi r G_c$. Finally, we take the limit as $\mathbf{a}$ approaches zero to obtain the following expression for the normalized peak applied strain:

$$\varepsilon_a^* = (8)^{1/2}\Bigg\{\left[\frac{7}{6}\right]\left[\frac{1}{\left(1+\frac{\phi}{\theta}\right)^2\sinh^3(\Psi\lambda)}\right]$$
$$\times \left[\left(-1+2\left(\frac{\phi}{\theta}\right)+\left(\frac{\phi}{\theta}\right)^2\right)\sinh(\Psi\lambda)\right.$$
$$+ 2\sinh(\Psi\lambda)\cosh(\Psi\lambda) - \sinh^3(\Psi\lambda) - \Psi\lambda$$
$$\times \left(\left(1+\left(\frac{\phi}{\theta}\right)^2\right)\cosh(\Psi\lambda) + \left(\frac{\phi}{\theta}\right)(1+\cosh^2(\Psi\lambda))\right)\Big]$$
$$+\left[\frac{\Psi\lambda}{\frac{\phi}{\theta}\left(1+\frac{\phi}{\theta}\right)\sinh^3(\Psi\lambda)}\right]\Big[\left(1+\left(\frac{\phi}{\theta}\right)^2\right)\cosh(\Psi\lambda)$$
$$\left.+\left(\frac{\phi}{\theta}\right)(\cosh^2(\Psi\lambda)+1)\Big]+1\right\}^{-1/2} \quad (35)$$

Because of the differentiation, the terms for the free lengths drop out of the final expression.

We can write eqns (33) and (35) more simply as follows:

$$\varepsilon_a^* = \left(\frac{8}{C}\right)^{1/2} \quad (36)$$

where constants C represent the quantities in curly brackets in eqns (33) and (35), and are designated C_{tot} and C_{crit} for the total energy model and the critical energy model, respectively. The values C will be referred to as the energy model parameters, and are dimensionless quantities.

Figure 5 shows the normalized shear stress for the center fiber at $\xi = 0$ plotted for four values of fiber volume fraction v_f over various values of θ around the center fiber to show the sensitivity in a realistic microcomposite of stresses to both of these parameters. The plots apply for both the total energy and critical energy models.

2.2 Analysis for the three-zone deformation model

In the three-zone model put forward by Gulino *et al.*,[8] the experimental basis for the existence of the three zones was set forth for the geometry of a planar array of three fibers. The center fiber was a carbon fiber, and the outer two fibers were much larger diameter glass fibers. These fibers were placed in a film of epoxy and strained. Breaks developed along the carbon fiber axis, and as the specimen strain was increased the breaks were studied locally for plastic yielding in the matrix, debonding at the interface and residual interfacial friction. At sufficiently high strain one would begin to see all three types of behavior, leading to three corresponding, distinct zones in succession as one moved along the fiber towards a break. The debonded zone with residual friction was closest to the fiber end and would tend to expand with increasing strain. Glass fibers were used to ensure that the strain to failure of the outer fibers would be much higher than the strain to failure of the carbon fiber. The glass fibers would continue to deform without fracturing while the carbon fiber fragmented, maintaining rigid constraints for the matrix next to the fiber breaks as they would occur in a real composite. Motivating the use of this model was the observation that epoxies behaved differently in small volumes and

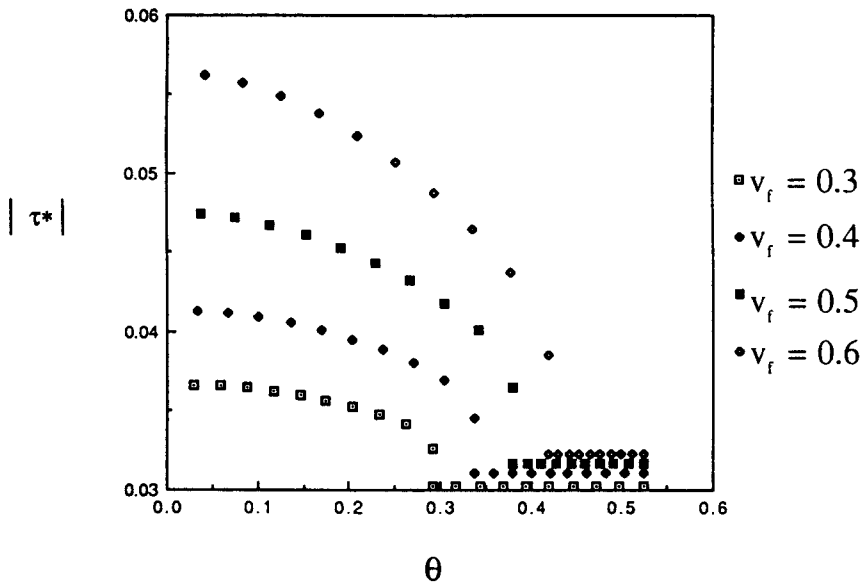

Fig. 5. Shear stress in the matrix at the interface calculated from eqn (21) with $\lambda = 20$ as it varies azimuthally, for various fiber volume fractions. (Note that the value of θ_{MAX} changes with fiber volume fraction, and that, at $\theta > \theta_{MAX}$, $b = b_{min} + 2r$.) Materials constants used are as in Section 3.

films compared with their behavior in bulk (where the epoxy could appear brittle), locally undergoing high, plastic shear strains before rapid strain hardening and sudden failure. With the assumption, then, that the locally high matrix strain, rather than an elastic analysis with a work of fracture approach, was the determining basis in the stress transfer and debonding, the epoxy's constitutive behavior in thin films rather than in bulk was used to model load transfer in the composite.

The geometry of the SFPOM experiment is somewhat different from the case of Gulino *et al.*,[8] but we would expect to see all three zones develop in succession along the fiber from $\xi = 0$ to $\xi = \lambda$ with increasing applied strain to the center fiber, provided that the embedded length λ is sufficiently long. This is shown in Fig. 6 in dimensionless terms where the key distances and positions along the center fiber are all normalized by the fiber diameter d as before in eqns (7), (8), (9) and (11). The governing differential equations for each of the three zones, elastic, plastic and frictional debond, follow from a simple balance of linear momentum on a small fiber element in each zone, assuming a shear-lag model with the appropriate matrix constitutive rule in respective zones. Initially, we assume that the normalized embedded length, λ, is sufficient for all three zones to coexist in some range of applied strain ε_a. The transition points μ and η represent the dimensionless boundaries between the elastic and plastic zones, and the plastic and debond zones, respectively, whose precise determination is given below.

General solutions for displacements and strains in the center and outer fibers are obtained for given

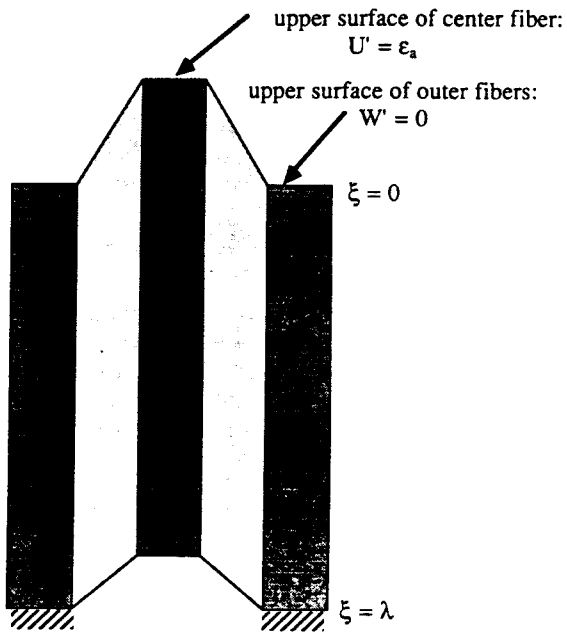

Fig. 6. Schematic of the three-zone model: idealized situation used for modeling, including expected axial constitutive zones for high embedded lengths.

transition positions μ and η between the respective zones. Later, shear strain criteria are used to calculate the length and growth of these zones as the displacement of the center fiber increases. The governing equations below are written as before in eqns (13) and (14) in terms of normalizations **U** and **W** of displacements u (center fiber displacement) and w (common outer fiber displacement), and are as

follows for the three distinct zones:

(I) Debond zone:

$$0 \le \xi \le \eta: \quad \mathbf{U}_\mathrm{I}'' - \alpha\tau_\mathrm{D}^* = 0 \tag{37}$$

$$\mathbf{W}_\mathrm{I}'' - \beta\tau_\mathrm{D}^* = 0 \tag{38}$$

(II) Plastic zone:

$$\eta \le \xi \le \mu: \quad \mathbf{U}_\mathrm{II}'' - \alpha\tau_\mathrm{Y}^* = 0 \tag{39}$$

$$\mathbf{W}_\mathrm{II}'' - \beta\tau_\mathrm{Y}^* = 0 \tag{40}$$

(III) Elastic zone:

$$\mu \le \xi \le \lambda: \quad \mathbf{U}_\mathrm{III}'' + 2\phi(\mathbf{W} - \mathbf{U}) = 0 \tag{41}$$

$$\mathbf{W}_\mathrm{III}'' + 2\theta(\mathbf{U} - \mathbf{W}) = 0 \tag{42}$$

where the double prime again denotes the second derivative with respect to dimensionless distance ξ, with the following definitions of parameters:

$$\alpha = 4\varepsilon_\mathrm{a} \tag{43}$$

$$\beta = -\frac{2}{3}\varepsilon_\mathrm{a} \tag{44}$$

$$\tau_\mathrm{D}^* = \frac{\tau_\mathrm{D}}{E\varepsilon_\mathrm{a}} \tag{45}$$

$$\tau_\mathrm{Y}^* = \frac{\tau_\mathrm{Y}}{E\varepsilon_\mathrm{a}} \tag{46}$$

where ε_a is the applied strain on the center fiber. Following Gulino *et al.*,[8] these parameters apply again to the special geometry where the six, surrounding fibers each have shear tractions applied through the matrix to only 60° of their circumferences and the center fiber has shear tractions applied over its entire circumference.

Compared with the description here, the transition zones may be less well defined in reality, as plastic and elastic, or debond and plastic zones may coexist around the circumference of the center fiber depending on the proximity of an outer fiber. In other words, the matrix material in the region where the surfaces of the inner and outer fibers are closest will be the first to yield or debond. The implications of these effects on the interpretation of pull-out data will be discussed below.

These six differential equations are solved with four boundary conditions at the dimensionless positions $\xi = 0$ and $\xi = \lambda$, namely,

$$\xi = 0: \quad \mathbf{U}_\mathrm{I}' = \varepsilon_\mathrm{a} \tag{47a}$$

$$\mathbf{W}_\mathrm{I}' = 0 \tag{47b}$$

$$\xi = \lambda: \quad \mathbf{U}_\mathrm{III}' = 0 \tag{47c}$$

$$\mathbf{W}_\mathrm{III} = 0 \tag{47d}$$

We also have eight continuity conditions in strains and displacements for the transition values $\xi = \mu$ and $\xi = \eta$, e.g. $\mathbf{U}_\mathrm{I} = \mathbf{U}_\mathrm{II}$ at $\xi = \eta$, etc. The general solutions for displacements and strains with arbitrary plastic and debonded zones are as follows:

Displacements:

center fiber:

$$\mathbf{U}_\mathrm{I} = \tfrac{1}{2}\alpha\tau_\mathrm{D}^*\xi^2 + \varepsilon_\mathrm{a}\xi + \tfrac{1}{2}\alpha(\tau_\mathrm{D}^* - \tau_\mathrm{Y}^*)\eta^2 + K_1 \tag{48}$$

$$\mathbf{U}_\mathrm{II} = \tfrac{1}{2}\alpha\tau_\mathrm{Y}^*\xi^2 + [\alpha(\tau_\mathrm{D}^* - \tau_\mathrm{Y}^*)\eta + \varepsilon_\mathrm{a}]\xi + K_1 \tag{49}$$

$$\mathbf{U}_\mathrm{III} = K_3\left\{e^{\Psi\xi} + e^{\Psi\lambda}\left[\frac{\theta}{\phi} - \Psi(\xi - \lambda)\right]\right\} + K_4\left\{e^{-\Psi\xi} + e^{-\Psi\lambda}\left[\frac{\theta}{\phi} + \Psi(\xi - \lambda)\right]\right\} \tag{50}$$

outer fiber:

$$\mathbf{W}_\mathrm{I} = \tfrac{1}{2}\beta\tau_\mathrm{D}^*\xi^2 + \tfrac{1}{2}\beta(\tau_\mathrm{D}^* - \tau_\mathrm{Y}^*)\eta^2 + K_2 \tag{51}$$

$$\mathbf{W}_\mathrm{II} = \tfrac{1}{2}\beta\tau_\mathrm{Y}^*\xi^2 + \beta(\tau_\mathrm{D}^* - \tau_\mathrm{Y}^*)\eta\xi + K_2 \tag{52}$$

$$\mathbf{W}_\mathrm{III} = K_3\left\{-\frac{\theta}{\phi}e^{\Psi\xi} + e^{\Psi\lambda}\left[\frac{\theta}{\phi} - \Psi(\xi - \lambda)\right]\right\} + K_4\left\{-\frac{\theta}{\phi}e^{-\Psi\xi} + e^{-\Psi\lambda}\left[\frac{\theta}{\phi} + \Psi(\xi - \lambda)\right]\right\} \tag{53}$$

Strains:

center fiber:

$$\mathbf{U}_\mathrm{I}' = \alpha\tau_\mathrm{D}^*\xi + \varepsilon_\mathrm{a} \tag{54}$$

$$\mathbf{U}_\mathrm{II}' = \alpha\tau_\mathrm{Y}^*\xi + \alpha(\tau_\mathrm{D}^* - \tau_\mathrm{Y}^*)\eta + \varepsilon_\mathrm{a} \tag{55}$$

$$\mathbf{U}_\mathrm{III}' = \Psi\{K_3[e^{\Psi\xi} - e^{\Psi\lambda}] + K_4[-e^{-\Psi\xi} + e^{-\Psi\lambda}]\} \tag{56}$$

outer fiber:

$$\mathbf{W}_\mathrm{I}' = \beta\tau_\mathrm{D}^*\xi \tag{57}$$

$$\mathbf{W}_\mathrm{II}' = \beta\tau_\mathrm{Y}^*\xi + \beta(\tau_\mathrm{D}^* - \tau_\mathrm{Y}^*)\eta \tag{58}$$

$$\mathbf{W}_\mathrm{III}' = \Psi\left\{K_3\left[-\frac{\theta}{\phi}e^{\Psi\xi} - e^{\Psi\lambda}\right] + K_4\left[\frac{\theta}{\phi}e^{-\Psi\xi} + e^{-\Psi\lambda}\right]\right\} \tag{59}$$

where the constants K_1, K_2, K_3 and K_4 are defined as follows:

$$K_1 = -\tfrac{1}{2}\alpha\tau_\mathrm{Y}^*\mu^2 - [\alpha(\tau_\mathrm{D}^* - \tau_\mathrm{Y}^*)\eta + \varepsilon_\mathrm{a}]\mu + K_3\left\{e^{\Psi\mu} + e^{\Psi\lambda}\left[\frac{\theta}{\phi} - \Psi(\mu - \lambda)\right]\right\} + K_4\left\{e^{-\Psi\mu} + e^{-\Psi\lambda}\left[\frac{\theta}{\phi} + \Psi(\mu - \lambda)\right]\right\} \tag{60}$$

$$K_2 = -\tfrac{1}{2}\beta\tau_\mathrm{Y}^*\mu^2 - \beta(\tau_\mathrm{D}^* - \tau_\mathrm{Y}^*)\eta\mu + K_3\left\{-\frac{\theta}{\phi}e^{\Psi\mu} + e^{\Psi\lambda}\left[\frac{\theta}{\phi} - \Psi(\mu - \lambda)\right]\right\} + K_4\left\{-\frac{\theta}{\phi}e^{-\Psi\mu} + e^{-\Psi\lambda}\left[\frac{\theta}{\phi} + \Psi(\mu - \lambda)\right]\right\} \tag{61}$$

$$K_3 = \frac{\varepsilon_\mathrm{a} + K_4\Psi\left[\left(1 + \frac{\theta\alpha}{\phi\beta}\right)e^{-\Psi\mu} + \left(-1 + \frac{\alpha}{\beta}\right)e^{-\Psi\lambda}\right]}{\Psi\left[\left(1 + \frac{\theta\alpha}{\phi\beta}\right)e^{\Psi\mu} + \left(-1 + \frac{\alpha}{\beta}\right)e^{\Psi\lambda}\right]} \tag{62}$$

and

$$K_4 = \frac{\left\{ \begin{array}{l} \alpha[\tau_Y^*\mu + (\tau_D^* - \tau_Y^*)\eta]\left[\left(\frac{\beta}{\alpha} + \frac{\theta}{\phi}\right)e^{\Psi\mu} \right. \\ \left. \quad + \left(-\frac{\beta}{\alpha} + 1\right)e^{\Psi\lambda}\right] + \varepsilon_a\left[\frac{\theta}{\phi}e^{\Psi\mu} + e^{\Psi\lambda}\right] \end{array} \right\}}{\Psi\left(1 + \frac{\theta}{\phi}\right)[e^{\Psi(\mu-\lambda)} - e^{\Psi(\lambda-\mu)}]} \quad (63)$$

It should be noted that the solutions above collapse to the much simpler solution of the system of eqns (13) and (14) when there are no plastic or debond zones present.

The lengths of the three zones along the embedded length are determined by shear strain criteria. We have, at each of the zone fronts,

$$\frac{U_{III} - W_{III}}{b_{eff}^*} = \gamma_Y \quad \text{for} \quad \xi = \mu \quad (64)$$

$$\frac{U_{II} - W_{II}}{b_{eff}^*} = \gamma_D \quad \text{for} \quad \xi = \eta \quad (65)$$

where $0 \leq \eta < \mu \leq \lambda$, $\gamma_D > \gamma_Y$, and b_{eff}^* is given by eqn (10).

As the applied strain is increased from zero, two critical strains will be achieved in the free length of the center fiber in succession, for sufficiently long embedded lengths. The critical strain at which a plastic zone initially develops in the matrix, ε_{ap}, will first be reached. Clearly, as $\gamma_D > \gamma_Y$, there will be no debond zone in the matrix at this point. The critical plastic strain, ε_{ap}, can easily be calculated by solving eqn (64) at $\xi = \mu = \eta = 0$ for ε_a, and setting $\varepsilon_a = \varepsilon_{ap}$. Subsequent straining of the center fiber will result in the axial growth of the plastic zone. Thus at strains somewhat larger than ε_{ap}, both a plastic and an elastic zone will coexist, with eqn (64) defining the boundary.

The next critical condition, at which debonding is initiated in the matrix, is given by eqn (65) at $\xi = 0$. Simultaneous solution of eqns (64) and (65) with $\eta = 0$ is required for determination of applied strain and length of plastic zone, μ, at this critical point; the ε_a obtained by this solution is ε_{ad}. At strains somewhat higher than this critical strain, all three zones can coexist along the fiber.

Coexistence of zones in a sample is governed largely by the embedded length. In long embedded lengths, we expect to be able to observe all three regions simultaneously. In extremely short embedded lengths, however, the plastic zone may encompass the entire length of the specimen before debonding begins. Thus, only two zones at a time may occur during an experiment, elastic and plastic zones for $\varepsilon_a < \varepsilon_{ad}$, and plastic and debond zones for $\varepsilon_a > \varepsilon_{ad}$. Coexistence of elastic and plastic, then plastic and debonded regions will occur only briefly over a small region of applied strain, the latter being unstable. For long embedded lengths, however, we expect to see all three zones develop with high enough applied strain.

The fiber volume fraction also plays an important role in the development of the different constitutive zones in the matrix material. At a given embedded length, a higher volume fraction specimen will exhibit a lower ε_{ap}, as the proximity of the stiff boundaries provided by neighboring fibers drives up the matrix elastic shear stress and shear strain at $\xi = 0$ and forces local yielding at a lower ε_a. Furthermore, for the higher fiber volume fraction specimens, the rate of fiber stress decay axially in the elastic zone is higher (through eqn (2)), thus making coexistence of debonded, plastic and elastic zones possible, as the plastic zone will not encompass the entire embedded length before local debonding is initiated at $\xi = 0$.

3 EVALUATION OF ANALYSES

The data from SFPOM experiments reported by Qiu and Schwartz[12] are fitted to the two energy-based expressions given by eqns (33) and (35) by using the normalizations contained by eqn (36). They are shown in Fig. 7. The fiber Young's modulus was reported to be 166·31 GPa (Kevlar 149), the matrix shear modulus was reported to be 525 MPa (70% Dow DER331, 30% DER732, 12·74 phr DEH No. 26 hardener).[12] Figure 7 clearly shows that the data do not support the energy approaches.

Simulations of the three-zone model derived here were also performed by using the data reported by Qiu and Schwartz[12] to assess its suitability. Simulations of each experiment performed with the three-zone model are plotted versus experimental results for failure strain in Fig. 8. It should be noted

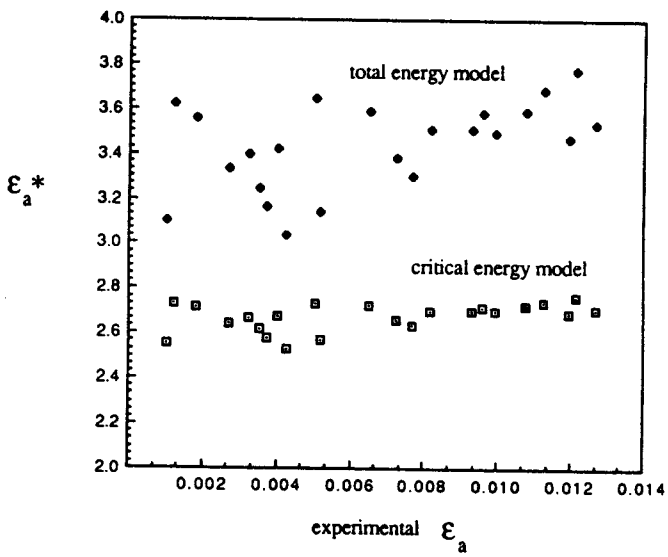

Fig. 7. Fit of experimental data to the total energy model, eqn (33), and to the critical energy model, eqn (35).

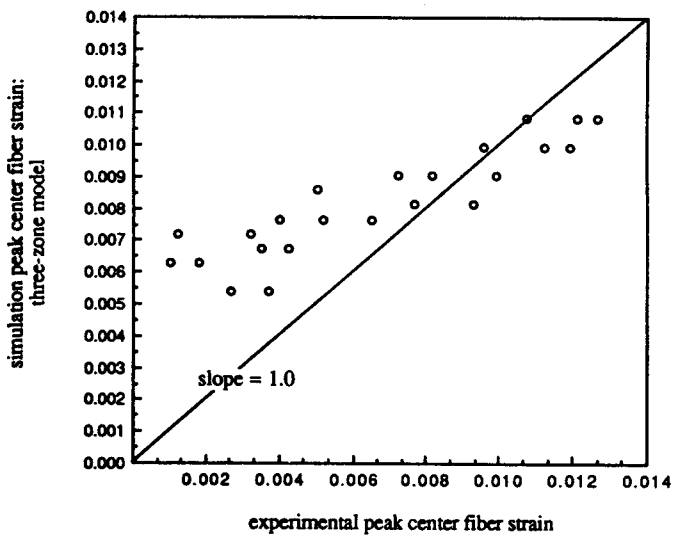

Fig. 8. Three-zone model simulation results for each experiment, with experimental results, for simulated center fiber peak strain vs experimental center fiber strain at failure with γ_Y assumed to be 0·055 and γ_D assumed to be higher than that reached at specimen failure. Materials constants used are as in Section 3.

that each point plotted in this figure represents a different fiber volume fraction and embedded length. Shear strain at yield for the matrix, γ_Y, was assumed to be 0·055 and debonding shear strain, γ_D, was assumed to be higher than that reached at the peak center fiber strain at failure; for the materials and geometry of the SFPOM specimens, a value of 0·30 was sufficient. Assumed values for τ_D^* and τ_Y^* were zero and $2{\cdot}53 \times 10^{-4}$, respectively (the latter quantity was chosen to insure continuity in the matrix constitutive law in the elasto-plastic region). Results for peak strain were not dependent upon τ_D^* provided $\tau_D^* < \tau_Y^*$.

4 DISCUSSION

The SFPOM experiment provides a more realistic setting in which to assess fiber/matrix interfacial properties than many other experiments currently performed. One of the advantages of the sample geometry is that the 'rigid wall' boundary condition is effectively simulated, because, as in real composites, the matrix is sandwiched between rigid fibers. That this situation differs markedly from the single-fiber experiments performed previously can be seen in Figs 2 and 5, which show that effective interfiber spacing is a critical quantity for shear stress calculation. Observation of the variation of shear stress with θ in Fig. 5 clearly shows that shear stress varies through small distances in even a moderately low fiber volume fraction microcomposite. This geometry may, in fact, better capture some of the 'interphase' effects reported in the literature.[13] Zones of varying compliance extending radially outward from the

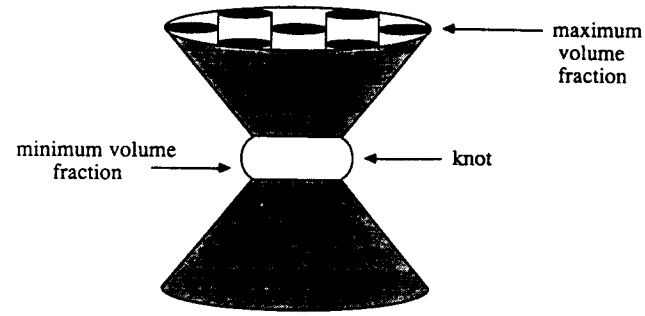

Fig. 9. Schematic of actual geometry of the SFPOM specimens.

center fiber may be better simulated in a microcomposite in which nearly impinging fibers (at high volume fraction) are present.

Mechanical modeling of the experiment, however, is problematic. As a consequence of the fabrication technique used by Qiu and Schwartz,[11] the specimens had a geometry resembling the exaggerated diagram in Fig. 9. Although the seven fibers were assumed to be axially parallel in the mechanical analyses in Section 2, the interfiber spacing actually decreased linearly from the top of the specimen to zero at the center of the specimen ($\lambda/2$). The result of such a variation is that the shear stress computed in a shear-lag model does not decay monotonically along the center fiber axially from $z = 0$ (see Fig. 1(b)). Instead, there is a competing effect in the specimen against shear stress decay, as the reduction in interfiber spacing at the knot increases shear stress, or equivalently, increases the effective shear modulus of the matrix, as seen by eqn (3). One expects that this 'spike' in shear stress will cause short specimens to fail by debonding initiated at the center of the specimen instead of at the top. In sufficiently long specimens, we expect this effect to subside, as effective shear stress and fiber load decay substantially axially before reaching the center of a specimen, where the spike becomes non-critical. This effect is illustrated in Fig. 10(a). The effect of this geometry on the resulting peak center fiber strain is illustrated in Fig. 10(b), with a schematic fit to the SFPOM data under the assumption that this effect plays a role in stress transfer.

This geometry effect would explain the negative intercept reported by Qiu and Schwartz[9,11] in a plot of pull-out load vs. embedded length for the SFPOM experiment. In the specimens used, higher embedded lengths were generally coincident with lower fiber volume fractions. Thus, in Fig. 8, the embedded lengths are higher and the fiber volume fractions are lower for the higher peak experimental loads, as is predicted by the three-zone model. However, the skew caused by this geometry effect is apparent. Although the three-zone model fits the higher

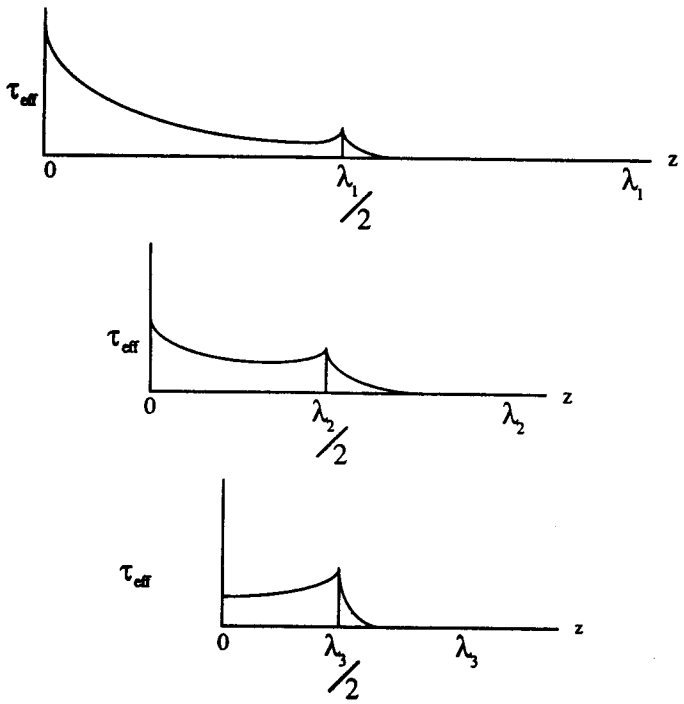

(a)

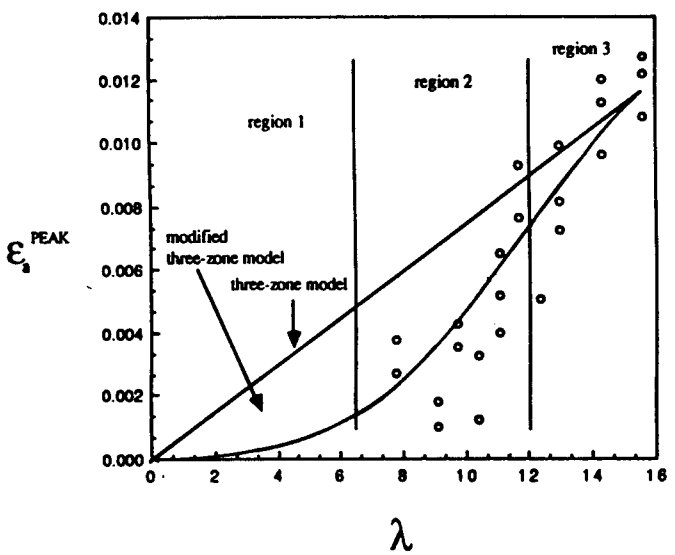

(b)

Fig. 10. Effect of the conical geometry in the SFPOM experiment on (a) axial shear stress decay, and (b) SFPOM data for peak center fiber strain for increasing embedded lengths.

embedded length data reasonably well at $\gamma_Y = 0{\cdot}055$, the lower embedded length data are overestimated with respect to ε_a^{PEAK}. In fact, the three-zone model is fitting a more simplified geometry (compare Figs 1(b) and 9).

Another view of this situation is shown in Fig. 10. Figure 10(a) illustrates the effect of the conical geometry on the shear stress distribution for three regions of embedded lengths. For sufficiently high embedded lengths such as λ_1, it is expected that the modification to axial shear stress distribution will produce only a small effect. For the shortest lengths, however, such as λ_3, the spike in shear stress is high enough to cause failure at very low ε_a because the peak shear stress is high whereas the area over which it acts is low. A sketch of the effect of the difference in behavior of the three regions of embedded lengths of Fig. 10(a) is drawn in Fig. 10(b), along with a result for the unmodified three-zone model, shown for a single fiber volume fraction.

The effects of debonding shear strain, γ_D, and fiber volume fraction in the three-zone model are illustrated by Figs 11(a) and (b). Materials constants are again as given in Section 3. The three debonding shear strains chosen represent a range of possible behavior in the model. If $\gamma_D = \gamma_Y$, as in the first curve in each plot, we see that the peak strain possible for any embedded length is limited to that reached for a matrix failing at its elastic limit. In the case of an intermediate γ_D, long embedded lengths will produce lower peak strains at failure than they would if γ_D were infinite, as a debonded zone is unstable, whereas the shortest embedded lengths show no difference in the two cases. The short embedded lengths are unaffected by increases in these intermediate debonding shear strains because the plastic zone in these cases encompasses the entire length of the specimen before even the moderate γ_D is reached at the top of the specimen, thus making the peak strain equal to that obtained by solution of eqn (64) at $\mu = \lambda$, with $\eta = 0$. At the highest debonding shear strains, even the long embedded lengths will behave in this manner, making the analysis of peak strains elasto-plastic. The effect of increasing fiber volume fraction in each of these cases is to lower the peak strain, as discussed in Section 2. Comparison of Figs 11(a) and (b) illustrates this effect for fiber volume fractions of 0·1 and 0·8.

The re-derived energy models of Piggott[5] and Penn and Lee[7] for the SFPOM geometry failed to model the experimental data with any degree of closeness, and have other deficiencies for use in strength simulations. Figure 12 shows the normalized analytic predictions for peak center fiber strain vs. normalized embedded length in the total energy model and critical energy model for 0·5 fiber volume fraction specimen, using the materials constants given in Section 3. The critical energy model shows an asymptotic approach to a constant value of peak center fiber strain with greater embedded lengths. However, for greater embedded lengths with an elastic matrix, one expects the peak center fiber strain to increase, reaching a constant only when the fiber ultimate strain is reached, at

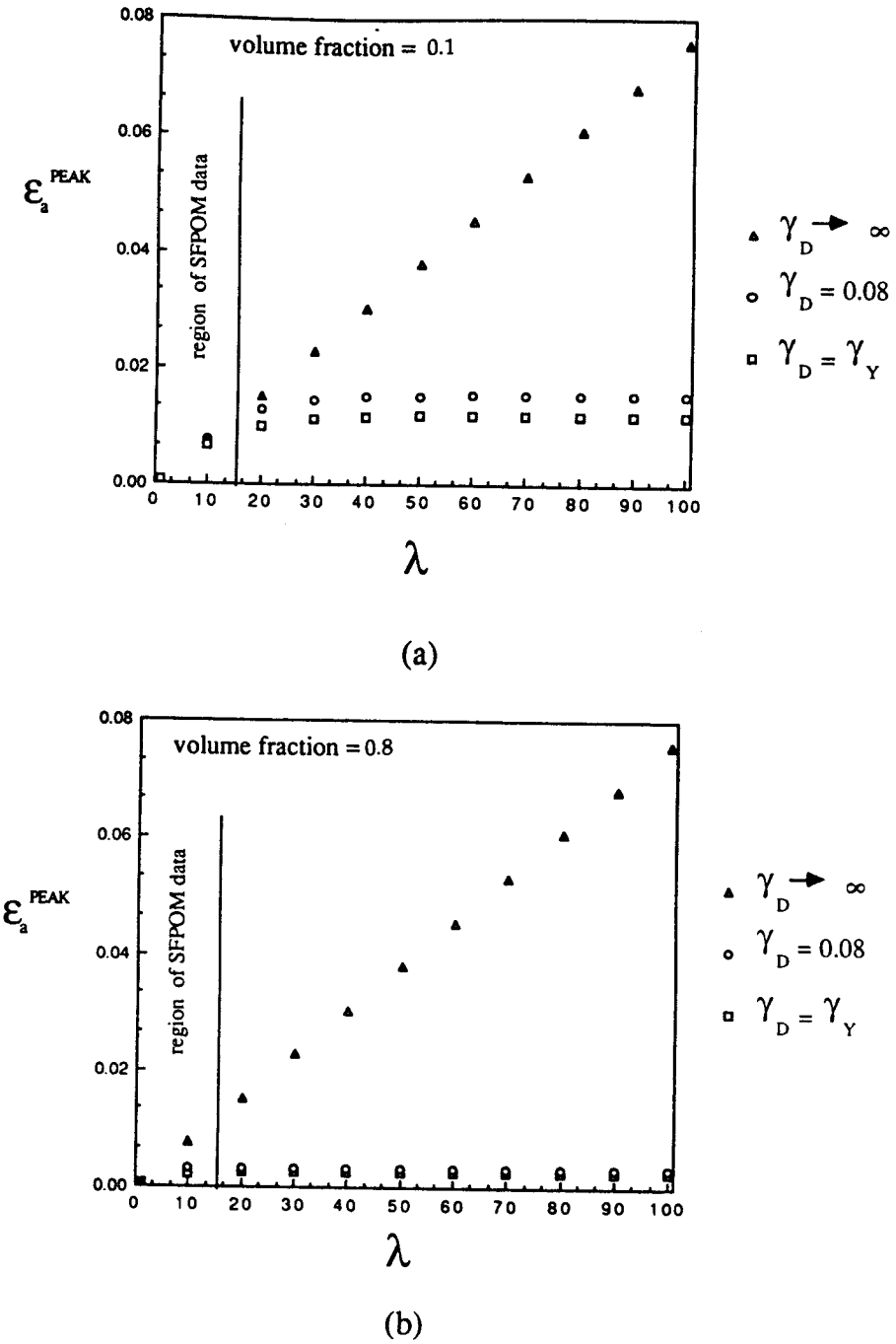

Fig. 11. Analytic predictions for peak center fiber strain for increasing embedded length for $\gamma_Y = 0{\cdot}055$ and $\gamma_D = \gamma_Y$, 0·08 and infinity for (a) a 0·3 fiber volume fraction specimen, and (b) a 0·6 fiber volume fraction specimen for the three-zone model. Materials constants are as in Section 3.

which point the center fiber itself fractures. There is no way to impose this 'critical length' on the resulting embedded length at which peak strain reaches a maximum in the critical energy model. Furthermore, Griffith-type approaches such as this are more appropriate in the case of brittle materials; the polymeric composites generally used in microcomposite experiments may exhibit large plastic deformations relative to the process zones of the debonded regions between fibers and matrix, relaxing the stress singularities which drive crack growth.

The total energy model, on the other hand, shows an ever-increasing peak center fiber strain with increasing embedded length. However, the primary assumption in this model, that a simple balance of energies at failure can be performed, suggests that a fracture takes place suddenly and catastrophically, regardless of materials or geometry. This method of

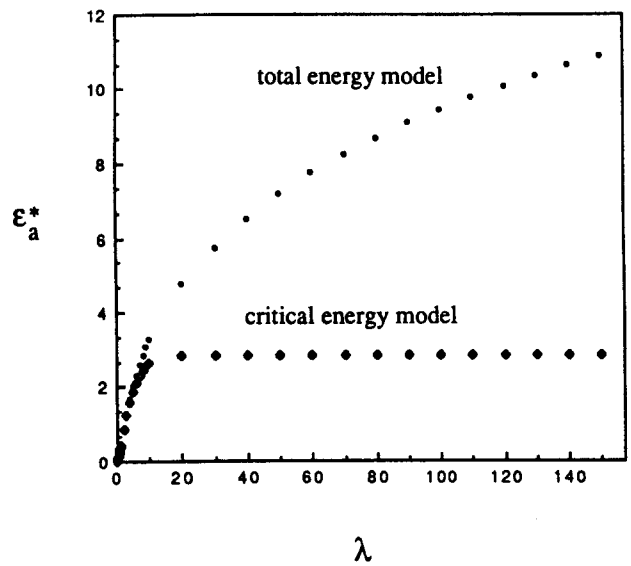

Fig. 12. Analytic predictions for peak center fiber strain for increasing embedded length for a 0·5 fiber volume fraction specimen for the total energy model and the critical energy model. Materials constants used are as in Section 3.

determining the failure criterion would suggest that the strength of any material can be calculated using a surface energy of a cross-section computed by balancing the stored elastic energy with work of fracture in a simple tension test, which is certainly not the case.

Piggott[10] recommended use of the critical energy model in analyzing brittle fracture processes with an equivalent debonding stress

$$\tau_D = [E_m(1+\nu_m)(G_c/r)\ln(R/r)]^{1/2} \qquad (66)$$

with R defined as the specimen outer radius and V_m is defined as the matrix Poisson's ratio. However, the possibility of coexistence of several constitutive axial zones in an interface was not considered in this approach. Furthermore, we have the persistent problem of a levelling of peak center fiber strain with ever-increasing embedded length.

Use of the three-zone model eliminates these difficulties. With this model, there are clear demarcations among relationships of peak center fiber strain to embedded length for a given fiber/matrix pair. Clearly, the fiber failure strain must be included as an additional limit in a strength simulation in the case of high embedded lengths. Unlike the result for the critical energy model, this analysis shows a monotonically increasing failure strain at higher embedded lengths. Parameters that determine the type of pull-out process are obtainable from experiments on constituents alone and combined in a microcomposite test such as that performed by Qiu and Schwartz[9] or Gulino *et al.*[8] Importantly, Gulino's verification of the three-zone model in an effectively two-dimensional specimen is further supported by Qiu's three-dimensional experiments.

5 CONCLUSIONS

Two interfacial fracture models adapted here for the experimental geometry were examined, and modified to account for the azimuthally varying shear stresses in the cross-section. It was shown that neither of the first two models fits the experimental data. Furthermore, there are several analytical problems with the use of these fracture models in a simulation of composite strength. Use of the fracture models derived here provided significantly different functional forms for prediction of peak center fiber strain, and failed to fit the experimental data for the SFPOM experiment.

A three-zone model of matrix constitutive behavior was also examined for use with the experimental geometry. The relationship between peak center fiber strain and embedded length for a short embedded length was fairly consistent with the analytical results. The model also lends itself to strength modeling in that the limits of high fiber volume fraction and high embedded length give reasonable solutions for developed strains in the matrix.

6 FURTHER WORK

The effects of unique geometry of the SFPOM experiment should be studied further both experimentally and analytically. The three-zone model should be modified to account for the conical geometry in the actual specimens, and the fabrication technique of specimens might be modified to produce a more cylindrical geometry, perhaps by using two knots to secure bundles instead of one.

ACKNOWLEDGEMENTS

The authors wish to acknowledge the helpful explanations given by Dr Yiping Qiu on his technique in performing the SFPOM experiments, as well as access to his experimental results.

REFERENCES

1. Herrera-Franco, P. J. & Drzal, L. T., Comparison of methods for the measurement of fibre/matrix adhesion in composites. *Composites*, **23** (1992) 2–27.
2. Cox, H. L., The elasticity and strength of paper and other fibrous materials. *Br. J. Appl. Phys.*, **3** (1952) 72–9.
3. Kelly, A. & Tyson, W. R., Tensile properties of fiber reinforced metals: copper/tungsten and copper/molybdenum. *J. Mech. Phys. Solids*, **13** (1965) 329–50.
4. Netravali, A. N., Henstenburg, R. B., Phoenix, S. L. & Schwartz, P., Interfacial shear strength studies using the single-filament-composite test I: Experiments on graph-

ite fibers in epoxy. *Polym. Composites,* **10** (1989) 226–41.
5. Piggott, M. R., Debonding and friction at fibre–polymer interfaces. I: Criteria for failure and sliding. *Composites Sci. Technol.*, **30** (1987) 295–306.
6. Chua, P. S. & Piggott, M. R., The glass-fibre polymer interface: I—Theoretical consideration for single filament pull-out test. *Composites Sci. Technol.*, **22** (1985) 33–42.
7. Penn, L. S. & Lee, S. M., Interpretation of experimental results in the single pull-out filament test. *Composites Technol. Res.*, **11** (1989) 23–29.
8. Gulino, R., Schwartz, P. & Phoenix, S. L., Experiments on shear deformation, debonding and local load transfer in a model graphite/glass/epoxy microcomposite. *J. Composite Mater.*, **26** (1991) 6655–72.
9. Qiu, Y. & Schwartz, P., A new method for study of the fiber–matrix interface in composites: single fiber pull-out from a microcomposite. *J. Adhesion Sci. Technol.*, **5** (1991) 741–56.
10. Piggott, M. R., Failure processes in the fiber–polymer interphase. *Composites Sci. Technol.*, **42** (1991) 57–76.
11. Greszcsuk, L. B., Theoretical studies of the mechanics of the fiber–matrix interface in composites. *ASTM STP,* **452** (1968) 42–58.
12. Qiu, Y. & Schwartz, P., Single fibre pull-out from a microcomposite test. *Composites Sci. Technol.* (in press).
13. Williams, J. G., Donnellan, M. E., James, M. R. & Morris, W. L., Properties of the interphase in organic matrix composites. *Mater. Sci. Eng.*, **A216** (1990) 305–312.